

Final Draft
of the original manuscript:

Stanev, E.V.; Al-Nadhairi, R.; Staneva, J.; Schulz-Stellenfleth, J.;
Valle-Levinson, A.:

Tidal wave transformations in the German Bight

In: Ocean Dynamics (2014) Springer

DOI: 10.1007/s10236-014-0733-6

Tidal Wave Transformations in the German Bight

Emil V. Stanev¹, Rahma Al-Nadhairi¹, Joanna Staneva¹, Johannes Schulz-Stellenfleth¹, and
Arnoldo Valle-Levinson²

Abstract

Mesoscale and submesoscale dynamics associated with tidal wave transformations were addressed in the German Bight using numerical simulations. Tidal gauge and velocity observations in several locations were used to validate the numerical model. A downscaling approach included analysis of simulations with horizontal resolutions of 1, 0.4 and 0.2 km. It was shown that the modified tidal wave lost most of its energy after reflection or refraction over the eastern part of the German Bight. Energy loss resulted in a pronounced change of the wave's spectral composition and generation of overtides. Tidal oscillations were modified by mesoscale processes associated with bathymetric channels. Semidiurnal and quarterdiurnal tides revealed very different spatial patterns. The former were aligned with the bathymetric channels, while the latter were rather "patchy" and had about half the spatial scales. In numerous areas around the bathymetric channels the major axis of the M_4 ellipses was normal or at some angle with the major axis of the M_2 ellipses. Thus, higher harmonics developed "orthogonal" patterns that drove secondary circulations. Moreover, the ratio between spring and neap tidal amplitudes was relatively low in the Wadden Sea, showing reduced sensitivity of this very shallow area to fortnightly tidal variations. It was demonstrated that simulated hydrodynamics patterns help explain the physical mechanism shaping the median grain size distribution in the German Bight.

¹Helmholtz Zentrum Geesthacht, Germany

²University of Florida, USA

1. Introduction

The tidal spectroscopy of shallow coastal areas and the associated effects of non-linear distortion and friction have been investigated extensively (Munk and Cartwright, 1966; Gallagher and Munk, 1971; Ianniello, J. P., 1977; Jay and Smith, 1990; Le Provost, 1991; Parker, 1991). The relative importance of various nonlinear mechanisms in distorting tidal waves can be summarized as follows: nonlinear advection terms are responsible for the generation of even harmonic overtides, for instance M_4 ; nonlinear friction is responsible for producing odd harmonic overtides, such as M_6 . Compound tides also arise in shallow waters as a result of the shallow-water interaction between two fundamental harmonics (e.g. M_2 and K_1).

In the European Shelf, aspects of tidal distortions have been addressed observationally with satellite altimetry and tide gauges (Andersen, 1999; Savcenko and Bosch, 2007). Most of earlier studies either addressed the problems theoretically or have overlooked the horizontal patterns of overtides at the transition between the coastal zone and the open ocean. This was a result of the data at the time not having the spatial and temporal resolution needed in the coastal zone.

There are two relevant geomorphological features in the coastal ocean with relatively small scales: (1) estuaries and (2) bathymetric channels. Bathymetric channels drain during ebb the water mass accumulated on the tidal flats during flood. These channels steer during flood the transport of ocean water into the coastal zone. Channels also provide a major link between terrestrial and marine systems, and represent a fundamental characteristic of the coastal ocean. To our knowledge most investigations on tidal transports in coastal areas concentrate on tidal estuaries, but little has been explored on their extension to the open sea. The main objective of

this study is then to analyse the coupling between estuaries and tidal flats, on one side, and the adjacent ocean, on the other.

Tidal waves are modified by advective nonlinearities and bottom friction as they move over tidal flats and toward the head of an estuary. In particular, the southeastern part of the North Sea (Fig. 1a) exhibits convergence of tidal energy in the corner of the German Bight. The Weser Estuary exemplifies a hyper-synchronous estuary (Allen et al., 1980; Nichols and Biggs, 1985) where the tidal range increases landward because tidal energy convergence dominates over friction. The case of Elbe Estuary, however, is more complicated. There, the tidal range decreases at the mouth (from location A to location B in Fig. 1b), then it increases and reaches a maximum of 3.5 m in the area of Hamburg, and decreases again to 2 m toward the weir in Geesthacht (Kappenberg et al., 1995, Eichweber and Lange, 1998; Plüß and Schüttrumpf, 2004).

The transformation in space and time of tidal waves in the coastal ocean and estuaries has indeed practical implications. Local variations in the major tidal constituents can produce tidal asymmetries, which are known to control the sediment dynamics in estuaries (Friedrichs and Aubrey, 1988). However this issue is less known for the areas connecting estuaries and the open sea. The study presented here could motivate future practical developments in the field of sediment dynamics of the German Bight and other similar coastal regions.

In the present study a three-dimensional numerical model was used to examine the spatial characteristics of overtides in the area of the German Bight. From existing local observations it is known that M_4 , M_6 , and MSF (period 14.77 days) are the most important overtides and compound tides in this region. Interpretations have also been provided on the dominant circulation and associated physical mechanisms. Further analyses have been carried out on tidal distortions related to M_4 and M_6 harmonics. Although very important, the river inputs

and meteorological forcing are included in the model but their effects are not considered here. This is the subject of a follow-up study.

This paper has been structured as follows: section 2 describes the region of investigation; section 3 presents the numerical model, model validation and general characteristics of the evolution of tidal constituents; section 4 depicts analysis of simulations; and this is followed by conclusions.

2. Study Area, Processes and Data Used

The German Bight shows nearly rectangular coastline with a funnel-like 30-40m deep Elbe valley crossing the area in a diagonal direction (Fig. 2a). The shoals off of the East Frisian Wadden Sea are steeper than those off of the North Frisian coast, the latter extending into the interior of the German Bight. To the east of the Helgoland Island the stone ground (*Steingrund*), a relict of an old moraine (Fig. 2 b), shows an underwater nearly zonal connection between Helgoland Island and the coast. As demonstrated in the present study, the *Steingrund* acts as an efficient barrier for wave propagation to the North and enhances the distortion of tidal signals. A sub-surface network of channels was not resolved in the coarse resolution map (Fig. 2a).

A Kelvin-like wave propagates around the North Sea coast in an anticlockwise direction with an amphidromic point at about 55.5° N and 5.5°E. Spatial distributions of the tidal constituents in the outer Elbe Estuary and German Bight have been proposed from relatively coarse numerical simulations and observations using HF radars (Carbajal and Polmann, 2004; Port et al., 2011). These studies demonstrated that the ellipse properties of the M_2 tide were strongly affected by coastal geometry and bottom topography. The dominant ellipse rotation

was anticlockwise with a reversal in the south-eastern corner of the German Bight and in the coastal embayments. Although these studies have addressed the interaction of tidal waves with the coastal geometry, the effects resulting from bathymetric channels have not been considered in the past because of insufficient resolution of the models and data used.

The Elbe Estuary consists of two regions: the upper region, which extends from approximately 9 °E upstream toward Hamburg Port (Fig. 2b, c), and the lower region (outer estuary or mouth) extending west of 9 °E. The latter displays a network of channels, with an average depth of $\approx 20\text{m}$, which includes the main estuary thalweg and several smaller secondary channels. To the west of the Elbe Estuary, the Weser Estuary and the Jade Channel (see also Fig. 1) have the most pronounced coastal and topographic features. The bathymetry of these estuarine extensions is also very complex. Basic physical processes in the inner Elbe Estuary, an M_2 tidally dominated system, have been reviewed by Kappenberg and Fanger (2007). This region shows a narrow channel with an average depth of about 15m and several tidal flats.

Data from long term tidal gauge stations as well as current meter data were used in the present study for model validation and interpretation purposes. Because the main interest here was the outer area of the estuary (the upper estuary will be subject to a follow-up study) data were extracted from the locations in Fig. 1b, which follow the main channels. Data were used also from other stations. The position of all stations used and their names are listed in Table 1.

3 The Numerical Model

3.1 Model Description

The General Estuarine Transport Model (GETM, Burchard and Bolding, 2002) was used in this study. This model solves the primitive equations for momentum, temperature, salinity and

water level. The model applied here uses the $k-\varepsilon$ turbulence closure to solve for the turbulent kinetic energy k and its dissipation rate ε . Horizontal discretisation was done on a spherical grid. The coarse resolution North Sea–Baltic Sea (3 nautical miles and 21 layers in σ -layers) outer model was described in more detail by Staneva et al. (2009); also see Fig. 6 of Stanev et al. (2011) for the maps of model domains. The sea surface elevation of the open boundary of the North Sea-Baltic Sea model was generated using thirteen tidal constituents (Annex 1) obtained from the TOPEX/Poseidon data via the OSU Tidal Inversion Software (Egbert and Erofeeva, 2002). The model was forced by atmospheric fluxes computed from bulk aerodynamic formulas. These formulas were based on model simulated sea surface temperature, 2 m air temperature and relative humidity together with 10m winds from atmospheric analysis data. This information was derived from the regional model COSMO-EU operated by the German Weather Service with a horizontal resolution of 7 km. River runoff data were provided by the German Federal Maritime and Hydrographic Agency (Bundesamt für Seeschifffahrt und Hydrographie, BSH). Temperature and salinity at the open boundaries were interpolated at each time step using the monthly mean climatological data. A set up for the German Bight based on the same model with about 1 km horizontal resolution was nested in the coarser domain model as explained by Staneva et al. (2009). Further downscaling to the scales of the Elbe Estuary was achieved with two nests in the German Bight model with 400 and 200 m horizontal resolution. The nesting was one-way.

All model configurations accounted for flooding and drying, which are fundamental dynamic processes in the Wadden Sea. Model configuration consists of an intertidal zone in the southeastern part of the North Sea between the coast and the Frisian Islands (Fig. 1a), forming a shallow body of water with tidal flats and wetlands. The bathymetric data were provided from the BSH. Mapping on regular grid was done in the Helmholtz-Zentrum Geesthacht.

While the resolution of 400 m seemed to resolve the major topographic elements in the outer estuary, it could not resolve the elements in the inner estuary (compare the insets in Figs. 2b and 2c). Both fine resolution grids extended to the Geesthacht Weir, the end point of propagation of tidal wave. Because of its insufficient resolution, the 1 km grid covered only the outer part of the Elbe Estuary. Hourly river discharge data was used for the Elbe (annual mean 787 m³/s) and Weser (annual mean 112 m³/s) Rivers. The simulations considered below provided results for the period April-May 2011, a period characterized by no extreme atmospheric conditions.

3.2 Model Validation

Surface elevation data were obtained every minute from the tide gauges network to validate the model simulations. Technical details on these data were available from the Federal Waterways and Shipping Administration (Wasser- und Schifffahrtsverwaltung des Bundes, <http://www.pegelonline.wsv.de>). Validation of numerical simulations against observations was performed at seven stations (Table 1). This was done in terms of phase and amplitude characteristics of the major tidal constituents computed with t-tide (Pawlowicz et al. 2002).

The analysis was restricted to the dominant diurnal and semidiurnal constituents (M_2 , S_2 , O_1 , K_1) and overtides (M_4 , M_6). Table A2 and Table A3 (Annexes) show that the smallest errors occur in the 200 m resolution model. The performance of the 400 m model was not as good as that of the 1 km resolution model, which was somewhat unexpected. This was an indication that the 400 m model could not resolve tidal distortion well enough in the estuary. The river part of the domain was not included in the 1 km model thus avoiding inconsistency from insufficient horizontal resolution in this area.

The 200 m resolution model simulations allowed a detailed scrutiny of the amplitude and phase patterns in the study area. The appropriate model performance also begged reconsideration of results from earlier simulations with models that could not resolve the dominant processes in the coastal zone. The agreement between these fine-scale simulations and observations was also very good in the open ocean (Fig. 3). The 200 m resolution model replicated the observed growth of tidal amplitudes in the estuary between stations 3 and 5. The match between the observed and simulated phases was also in very good agreement, illustrating the signal delay upon approaching the estuarine mouth.

Results of harmonic analysis of surface currents (Table A4) were compared between stations LZ₄ and Jade. It became clear that the major axes currents simulated with the 200 m resolution model agreed better with observations than those with the 400m resolution model. This justified the use of 200 m resolution simulations to describe the patterns of tidal constituents in the German Bight and Elbe Estuary. Some differences between simulations and observations did not disqualify the model as a tool for sensitivity analysis, but rather called for a deeper consideration of the fine-scale processes and fine-scale features of topography and coast in operational models. From other similar validation exercises (e.g. Fanjul et al., 1997) it is also known that some of the discrepancies between observations and models can be explained by the fact that some coastal gauges are in the interior of bays or at island lees. In such areas, locally generated topographic effects are not properly resolved even with a 200 m resolution.

4. Analysis of Numerical Simulations

4.1. Tidal Analysis of Water Elevation

Results from tidal harmonic analysis (Pawlowicz et al., 2002) of model output during April and May are discussed in this section. Illustrations are presented mostly for spring tides because they were most informative about nonlinear transformations of tides. These transformations reveal appreciable changes in the horizontal patterns of the major tidal constituents.

The co-phase and co-range lines simulated in the models with 1 km and 200 m resolution (Fig. 4) illustrated the dominant horizontal patterns of M_2 tide, which displayed the well-known distribution for the area phase and amplitude related to a Kelvin wave. The distance between two co-phase lines increased constantly from the amphidromic point (outside the model German Bight area) toward the coast. Furthermore this distance between co-phase lines increased from the western model boundary toward the Elbe mouth, as seen in Fig. 4a as a “divergence” in co-phase lines.

There was a sharp bending in the M_2 co-phase lines from normal to the coast in the open sea to aligned with the coast in the coastal zone (Fig. 4a). This was indicative of the delay of the tidal wave in the whole region from the Jade Channel to the Eider Estuary. Similar bending was simulated also off the Ems Estuary and Rømø Bay. The fact that this distortion in the tidal signal was not observed off the East Frisian Islands, i.e., from the Ems Estuary to Spikeroog Island, indicated that the orientation change was caused by the transformation of the tidal wave approaching the entrance of estuaries and bays. This supported earlier results of Carbajal and Pohlmann (2004), who concluded that tidal properties underwent major changes in zones of influence of embayments.

The amplitude of M_2 tide increased continuously toward the German Bight corner in the south-eastern part of the domain. Tidal amplitudes were greatest to the south of Helgoland Island, extending from the East Frisian Wadden Sea to the North Frisian Islands (Fig. 4a).

The patterns of the M_4 tide (Fig. 4b) demonstrated that the spatial scales were two times smaller than those of the M_2 tide, which agreed with the concept of doubling frequency and wave number in the generation of higher harmonics. There are two maxima, one at the southwestern part of the open boundary and another one along the North Frisian coast separated by a zone of low amplitudes, extending in the meridional direction to the east of the Ems Estuary. The patterns in Fig. 4b characterise the North Frisian Wadden Sea as the region of strongest generation of overtides with a maximum off the Eider Estuary. This result indicates that the reflection and refraction of a Kelvin wave in these regions is accompanied by clear distortions of the tide, thus enhancing the overtides.

Upon approaching the coast from the open ocean, the drop of tidal amplitude simulated by the 1 km resolution model displayed contrasting patterns in different parts of the Wadden Sea. Although the resolution of this model was sub-optimal for this part of the domain, some results were noteworthy. In general, the amplitude of M_2 tide decreased in the Ems, Jade and most of the North Frisian tidal basins. One exception was the Sylt-Rømø Bay. However, the most notable exception was the area off of the Weser and Elbe estuaries, where the tidal wave amplitude remained high. The combined effect of deeper topography, the narrowing of the coastline, and the convergence of tidal energy in the German Bight corner explained this local amplification of the M_2 tide.

In the fine resolution model the co-phase lines generally followed the shape of the corresponding lines in the 1 km model. However the pattern of amplitudes in the fine resolution model displayed more detail than the 1 km model (compare the isolines in Fig. 4a and c). Obviously, the bathymetric channels and coastal topography off of the river mouths allowed development of small-scale patterns, which were well defined in the tidal amplitude. There was also a marked delay in the tidal wave along the Elbe River between Cuxhaven and the area of bifurcation of the Elbe Channel, measured by the distance between individual

phase lines. In the same area the tidal amplitude decreased, which was known from the observations and earlier numerical simulations (Plüß and Schüttrumpf, 2004). After reaching a minimum in the area of the estuarine turbidity maximum (ETM, see Fig 1b for its location), the tidal amplitudes increased further in the direction of Hamburg Port. Tidal propagation in the Weser Estuary was different as no substantial delay was observed in the phases (compare the phase lines in Weser and Elbe Estuaries, Fig. 4c) and the tidal range in the estuary remained high along the entire estuary. The difference between the two estuaries was in the bending of the Elbe Channel and its bifurcation east of Cuxhaven. The Weser Estuary was geometrically simpler. For Jade Bay, the deep and wide channels connecting the bay with the open sea ensured an increase in the amplitude of the M_2 (amplitude about 1.4 m). These large amplitudes in Jade Bay and Wesser Estuary were also caused by the specific coastal geometry (converging coastlines), which resulted in focussing tidal energy landward. Therefore, the tidal amplitude in both Jade and Wesser increased toward the head of estuary (embayment), while in the Elbe River mouth (but not in the upper channel) it decreased because of bottom friction.

The large-scale pattern of the M_4 amplitude in the fine resolution simulations (Fig. 4d) follows the basic characteristics in Fig. 4b. The major difference between the two models is in the estuarine area, where the artifacts simulated in the 1 km resolution model (low amplitudes extending almost all the way down from the Jade Bay to Elbe Estuary) disappeared in the 200 m resolution model.

4.2. Tidal Analysis of Surface Currents

4.2.1 The 1 km Resolution Model

Tidal analysis of surface currents revealed spatial changes of patterns of the major tidal constituents (Fig. 5). The rough-scale (1 km resolution) maximum of M_2 tidal current was in the southwestern part of the domain, indicating the origin of the incoming tidal wave. The greatest M_2 currents followed the southern coast reaching the Elbe Valley south of the Helgoland Island. Most of the tidal energy remained trapped (reflected or dissipated) in the south-eastern German Bight and could not efficiently propagate over the shallow shelf off of the North Frisian Islands (see Fig. 2a). This interpretation was supported by Fig. 4a showing an asymmetry between Kelvin waves that enter and leave the German Bight. The amplitude in the southwestern part of the model area (the incident wave) was much larger and covered much wider area than the amplitude in the northeastern part (the outgoing wave). More specifically, this could be seen from the shape of the largest amplitudes (the first two dashed isolines in Fig. 4a originating from the western model boundary), which did not penetrate to the North of Sylt Island. As discussed later, the southern German Bight was dominated by a nearly zonal orientation of the tidal ellipses. This orientation could indicate that wave reflection from the eastern coast was pronounced and the M_2 energy was not efficiently redirected to the north. Therefore, meridional oscillations in the eastern part of the domain were reduced.

The overtides along the western model boundary showed amplitudes <0.04 m/s (Fig. 5c), but increased to the East (in a triangle-shaped area). The second area with large M_4 currents on the eastern shelf (Fig. 5c) was separated from the southern triangle-shaped area by a zone of low M_4 velocities extending in the northwest direction along the Elbe Valley.

If non-linearities were absent, the magnitudes of overtides would decrease within the estuary from their small offshore values. Like in the estuarine case (Aubrey and Speer, 1985) the amplitudes of overtides steadily increase and showed unknown patterns, which shed new light on the non-linear transformations of tides in the German Bight. In particular, the results

presented above revealed the areas where the incident wave generated overtides upon approaching the eastern coast. Furthermore, it became clear that while the M_2 magnitudes along the northern part of the eastern coast were relatively small, the M_4 magnitudes were relatively large (compare Fig. 5a and Fig 5c). One could conclude that after reflection or refraction over the eastern part of the German Bight, the modified tidal wave lost most of its energy. This energy loss resulted in a pronounced change of the wave's spectral composition. Similar decrease of tidal velocity oscillations along the eastern coast of the German Bight has been observed with HF radars (Schultz-Stellenfleth, personal communication).

The patterns in Fig. 5a, c correlate very well with the permeability pattern of marine sediments described by Janssen et al. (2005, see their Fig. 8). This correlation could be considered a fundamental link between hydrodynamics and biogeochemistry (more specifically sediment dynamics) in the German Bight. These authors estimated the permeability for the entire German Bight based on median grain size and sorting of 16,000 surface sediment samples. Their Fig. 8 actually revealed a dominance of sandy sediments in the area where simulations showed maxima of tidal current amplitudes off the East Frisian coast. In other words, high-energy flows support the transport and deposition of coarser sediment fractions (which is well known in sediment dynamics), that is also characterized by higher respiration rates. The analysis demonstrated that the dominant physical mechanism was replicated well by the model, which translates into a consistent explanation of basic features in sediment dynamics and biogeochemistry of the German Bight.

Not only the bottom sediment characteristics depend on tidal currents, they also depend on tidal asymmetries. Asymmetries in turn depend on the repartition of tidal constituents. In the southern part of the German Bight the high energy M_2 tide (Fig. 5a) is influential for the sediment distribution. Off the North Frisian Wadden Sea, sediment sorting is determined by the asymmetry associated with the increasing magnitude of the M_4 tide (Fig. 5c). The

seemingly different balances controlling the sediment dynamics in different parts of the German Bight could be considered as “symptoms” that identify plausible explanations and allow predictions.

Transformations of the tidal signal in the near-coastal area were characterized by multiple M_4 maxima in and around the narrow straits connecting the Wadden Sea and the open ocean, as well as in the major estuaries and embayments (Fig. 5c). This was to be expected because tidal distortions were generated mostly in the shallow areas. One example was around the *Steingrund* (see also Fig. 2b), which emulated an efficient barrier. Such blockage resulted in energy reduction of the northward wave. What seemed unexpected was the narrow band of low M_4 currents encompassing the entire coastal area in front of the barrier islands. This band was identified in almost the same area by Zeiler et al. (2000) as the sediment bypassing and depletion area. Postma (1984) introduced the notion of the “line of no return” when discussing the exchange of sediment between the Wadden Sea and German Bight. It was assumed that the line of no return was intimately connected to the observed suspended particulate matter minimum zone in front of the barrier islands. Particles beyond the line would unlikely be transported toward the Wadden Sea.

The amplitudes of the M_6 major axis surface current displayed a relatively simple horizontal pattern (Fig. 5e). Small magnitudes appeared in the open sea and large amplitudes appeared in the channels of the southern coast and in the areas in front of the estuaries. These were the regions of strongest M_2 tidal currents and where non-linear friction played the major role. It was also clearly seen that the Helgoland Island was a major source of friction, which extended in the downstream direction.

A comparison between the tidal analyses carried out separately for spring and neap periods with the results presented above (not presented here graphically), showed consistent spatial

structures but differences in the magnitudes. The M_4 tidal flow was much lower during neap, in particular over the eastern shelf. Although the 1 km run gave overall physically reasonable results, some patchy patterns indicated that further downscaling of the tidal variability was needed.

4.2.2. The 200 m Resolution Model

The fine resolution model showed a very different picture from the 1-km resolution model (Fig. 5 b, d, f). The flow was clearly influenced by the bathymetric channels. Semidiurnal tidal current amplitudes showed that the major channels (of Jade, Weser and Elbe) acted as the main transport avenues to and from deep waters. The magnitude of the M_2 major axis decreased markedly over the shoals that separate individual channels.

The pattern of the M_4 flow (Fig. 5d) occasionally showed minima in the channels. This was very clear in the Weser Estuary and Jade Channel. In general, amplitudes of M_4 flow were lower in the channels than over the tidal flats.

It was not only the overall distribution of amplitudes of M_2 and M_4 tides (opposite in the channels) but also the horizontal patterns and their characteristic scales, which differed largely between the two harmonics. Beyond the tidal flats, which undergo substantial flooding and drying (this is identified in Fig. 5 a, b, and c by the white areas), the M_2 amplitudes “follow” the under-water channels while the M_4 amplitudes reveal patchy structures. The most important feature of the M_4 velocity pattern was the spatial scales, which were half those of the M_2 . The larger number of isolated areas of M_4 maxima and minima in comparison to the M_2 distributions indicated that both the frequency and the wave number doubled in the M_4 tide. This is consistent with theory: if the phase speed of long gravity waves remains constant,

the ratio between wave number and angular frequency has to remain constant, too. The physical consequences of wave number transformations in the area are explained in the following sections.

Other small scale features dominated the shallow coastal area, for instance the maxima along the right bank of Jade Channel. These patterns result from small-scale topography elements that promote “overshooting” of the flood currents from the Jade Channel over the flats in the direction of Weser Estuary. Similar (oriented normally to the main channels) maxima were observed along the small channels connecting the tidal flats with the major channels (see the secondary channels in the topography map in Fig. 2).

Unlike the case of the M_4 tide, the pattern of M_6 major axis surface current (Fig. 5f) revealed clearly that the largest magnitudes were located in the deep channels where velocities were strongest and friction was highest. This harmonic did not show a pronounced magnitude on the tidal flats because velocity there was much lower than in the channels (opposite to the case of the M_4 tide).

4.2.3. Tidal Distortion

Non-linear forced tides are negligible in the open ocean, but are enhanced in semienclosed basins. The M_4 constituent amplifies over the estuary, indicating an increasing energy transfer from M_2 constituents to overtides. Thus, the M_4/M_2 ratio is a primary indicator of nonlinearity, which represents the effect of spectral energy transfer from M_2 to M_4 (Speer, 1984). This is similar in the German Bight (a giant estuary). In the bight, the ratio between the major axis amplitudes of M_4 and M_2 currents (M_{4amp}/M_{2amp}), as well as that between M_6 and M_2 (M_{6amp}/M_{2amp} , Fig. 6) give an idea on spatial characteristics of tidal distortions.

Ratios of $M_{4amp}/M_{2amp} > 0.2$ revealed areas of enhanced distortion of the tide. The most prominent large-scale area was noted in the north-eastern German Bight, where the M_4 current reached about 20% of the M_2 . This area coincided with the zone of refracted Kelvin waves, which suggests the following concept. Most of the German Bight was dominated by a relatively low M_{4amp}/M_{2amp} ratio; the overtide M_4 currents were about 7-10 times weaker than M_2 currents over most of the German Bight (Fig. 6a). Along the northern part of the eastern coast the M_{4amp}/M_{2amp} ratio increased, a result of the M_2 decrease at the refracted Kelvin wave in the northern part of the model area (see also Fig. 5a). This, along with an approximately negative correlation between M_{4amp} and M_{2amp} (Fig. 5c), explained the maximum in the distortion pattern (Fig. 6a). Noteworthy is the geometrical similarity between the simulated tidal asymmetries and the properties of bottom sediments of the North Frisian coast described by Janssen et al. (2005). Additionally to the mechanism proposed in section 4.2 relating the tidal energy to sediment distribution (off the southern coast), the M_{4amp}/M_{2amp} ratio can also be considered as a reason for shaping the pattern of median grain size in the German Bight, but mostly in its eastern part.

The tidal distortion was extremely large in the entire Wadden Sea. In this area the tidal range approached the water column depth and the impact of non-linear dynamics increased (Stanev et al., 2007). The latter was illustrated in Fig. 6a by the relative increase of amplitudes of M_4 currents compared to M_2 . There was a pronounced minimum of the M_{4amp}/M_{2amp} ratio in front of the barrier islands (more pronounced off the southern coast) followed by an offshore increase. This asymmetry is in the area of the sediment bypassing and depletion (Zeiler et al., 2000) and where the “line of no return” was reported by Postma (1984).

There is a substantial distortion also over the Steingrund, which illustrated how the small-scale topographic features modified tidal waves. In turn, the pattern of distortion associated with the M_6 current (caused mostly by non-linear friction) followed the general bathymetric

features. This was illustrated by the extension of areas of coastal maxima in front of the eastern coast, which was related to very shallow topography there (Fig. 2a).

The fine resolution simulations demonstrated the role of the channels and tidal flats. The M_4/M_2 pattern revealed large distortion reaching 0.3 on tidal flats shaped by the small-scale topographic features there (Fig. 6b). In contrast, tidal channels showed low M_4 amplitudes compared to M_2 . The distortion associated with the M_6 tide displayed less dependence on the local depth. The overall feature in Fig. 6d was the minimum zone in the north-western part of model area (south of Helgoland Island) and the larger values elsewhere (note that the color bars in all panels of Fig. 6 were the same). Some important details were striking: the Weser Estuary showed the maximum M_6 distortion while the distortion in the major channel of the Elbe River was small. However, in the northern (shallower) branch of the Elbe Channel, as well as in the whole flat area North of the Elbe River mouth, the effect of non-linear friction was very pronounced.

4.2.4. Transport of Tidal Energy

The above analysis of tidal spectrum evolution is summarized below focusing on the propagation of tidal energy. It is assumed that the water level associated with a tidal wave at some point is given by $\eta = \eta_0 \cos(\omega t - \Phi_\eta)$ with a corresponding current $u = u_0 \cos(\omega t - \Phi_u)$. Then the average energy flux per unit width over a tidal cycle is given by Pugh (1996) as

$$F = 0.5 \rho g D \eta_0 u_0 \cos(\Phi_\eta - \Phi_u), \quad (1)$$

where g is acceleration of gravity, D is water depth, and ρ is water density.

The basic transport patterns in Fig. 7 support the descriptions shown above. The energy flux associated with M_2 follows the southern coast until the wave reaches the shallow coastal zone.

There is almost no redirection of energy to the North. The fine resolution model demonstrates that the topographic channels provide the major pathway for M2 energy to penetrate in the estuaries. Recall that the non-linear spectral transfer accounts for only a small fraction of the total energy decay of M2, the larger portion is attributable to frictional dissipation (Speer, 1984). Obviously, the coastal area addressed in this paper provides this dissipation capability.

4.3. Tidal Ellipses

Tidal ellipses in the German Bight have been described on the basis of observations and numerical modelling but with a relatively coarse resolution (Carbajal and Pohlmann, 2004; Port et al., 2011; Stanev et al., 2011). The present simulations with 1 km resolution support earlier estimates revealing that over most of the German Bight areas, the M₂ tidal ellipses rotated counter clockwise (CCW, Fig. 8a). Only in front of the Ems and Elbe Estuaries, as well as in a small area along the western boundary, ellipses rotated clockwise (CW). As shown in Fig. 4, off the Ems and Elbe Estuaries the tidal wave underwent a delay (phase lines bent substantially). This indicated that the dominant balances between Coriolis force, pressure gradient and bottom friction changed, which altered the direction of rotation (see Carbajal and Gaviño, 2007 for further physical explanations of this effect).

The comparison between the M₂ tidal ellipses in the coarse and fine resolution models (Fig. 8a and Fig. 8b) demonstrated that in the overlapping area the two models gave similar results. However, the alignment of the M₂ ellipses along the channels in 200 m model was not seen in the coarser resolution model simulations (the grey colors indicated the position of the tidal channels). The alignment was neither seen with the M₄ tidal ellipses, an expected result as discussed in the previous section. In many areas the M₄ major axis was normal or showed some angle with respect to the M₂ ellipses, illustrating that the higher harmonics could reveal

“orthogonal” patterns and drive secondary circulation. As far as the M_6 ellipses were concerned, their direction correlated well with those of the M_2 because both oscillations were very strongly steered by the tidal channels.

4.4. Spring versus neap spatial variability

It is trivial to expect higher spring tidal amplitudes than in neap over the model area. However, the differences between their respective horizontal patterns, in particular those of the higher-order harmonics, were not so obvious. The ratio between spring and neap M_2 amplitudes (Fig. 9a) exhibited the largest values close to the open boundaries. Upon approach to the corner of the German Bight and the Wadden Sea, the enhancement of M_2 spring tide decreased, suggesting a reduced sensitivity of this area to the spring-neap cycle. The pattern in Fig. 9a was indicative of spatial changes associated with the magnitude of tidal forcing; maxima were observed at the open boundary along the southern coast and in the northeastern corner of the domain. The minimum zone followed the diagonal of the model area in the direction of the Elbe Estuary. While in the open sea the ratio of spring to neap amplitudes was above 1.3, in the Wadden Sea it contracted to 1.15 or less. This reduction was caused by greater frictional damping during spring tides (stronger currents).

The spatial patterns of the ratio between M_4 spring and M_4 neap tidal amplitudes (Fig. 9b) were very different from the M_2 tides. Similarly to what has been described in Fig. 4a, b, not only were the temporal scales of M_4 tides two times shorter than the M_2 tides (which is obvious), but also the spatial scales of the ratio between M_4 spring and M_4 neap tidal amplitudes were two times smaller (compare Fig. 9a with Fig. 9b). The zones of largest M_4 ratios, as compared to those of the M_2 tide, were found in the southwestern and northeastern corners of the model area. Together with the minima zones close to the northwestern open

boundary and southeastern coast, the overall pattern revealed a quadrupole shape. The maximum enhancement of M_4 spring tide was about 2.6 times; its lowest values in the open sea were about 1.5. While the corresponding M_2 ratios were never bigger than 1.5, the corresponding M_4 ratios changed over a wider range. This indicated that (1) M_4 tide associated with the non-linear processes was much more sensitive to spring-neap cycle than the M_2 tide, (2) the region most sensitive to spring-neap cycle was north of Sylt. It is expected that in this region, where the tidal asymmetries were very sensitive to neap-spring cycles, other processes (e. g. sediment dynamics) will also be sensitive to fortnightly variations.

The relatively low M_4 -ratios in the Wadden Sea, similarly to the case of the M_2 tide, showed less sensitivity to neap-spring differences. This shows that the barrier islands shield intertidal basins from the open ocean. The minimum amplification of the spring-to-neap signal was therefore found in the Wadden Sea.

The ratio between the spring and neap M_4 tide in some areas (e. g. the sharp change in the patterns in front of the Elbe and Weser mouths) may be affected by resolution problems in the simulations with the 1km model. As seen in the results of numerical simulations with 200 m resolution (Fig. 9 c, d), the case with the M_2 tide was overall similar to that of the 1 km model run: a decrease in ratio with decreasing distance from the coast in the corner of German Bight. However, the 200 m resolution model clearly demonstrated that the spring versus neap amplification decreased slightly in the estuaries, reaching lowest values over the tidal flats. Furthermore, the above mentioned artifacts in front of the Elbe and Weser estuaries produced by the 1 km model were not present in the 200 m simulations. With the latter horizontal resolution the simulated ratio between spring and neap M_4 tides decreased smoothly over the tidal flats and in the estuaries, demonstrating the near-coastal zone tends to “smooth” neap-to-spring variability in the region studied. Noteworthy is that this decrease was consistent with the observations (see Fig. 3), revealing that the spring to neap M_4 ratio changes from 2 at

location 1 to 1.4 at location 4 (see Fig. 1b for the locations). Both observations and numerical simulations demonstrated that for the same locations the spring-to-neap M_2 ratio was smaller (about 1.3) and did not change much.

5. Conclusion

The tidal spectroscopy in the German Bight has been presented on the basis of the analysis of observations and numerical simulations. Numerical simulations provided a useful tool to describe the spatial variability over areas that were not sufficiently sampled. Thus, these results shed new light on the spatial variability of tides and overtides outside estuary mouths. More weight in the discussion was given to the tidal composition around bathymetric channels, which could have an important practical implication because these topographic features provide a major link between terrestrial and marine systems. Thus, the present research also contributed to understanding the coupling among estuaries, tidal flats and the Southern North Sea. Another important practical aspect was that local variations in the major tidal constituents can affect tidal asymmetries and their associated sediment dynamics in the coastal zone.

The evolution of the tides in the German Bight was well illustrated by the delay of the tidal wave, mostly along the southern coast. In this area the amplitude of M_2 tide (the incident Kelvin wave) decreased considerably and the amplitude of the outgoing wave remained relatively small, thus M_2 energy was not efficiently redirected to the north. This energy loss resulted in a pronounced change of the wave's spectral composition. The eastern coast showed a substantial increase of the energy of overtides illustrating that reflection and refraction of M_2 tide was accompanied there by an intensification of the non-linear transfer of tidal energy and generation of higher harmonics.

Along the southern coast the change in spectral composition led to the local minimum in tidal distortion. Such minimum in distortion could be considered a candidate to explain the “line of no return” known from regional sediment studies and explaining the observed minimum zone of suspended particulate matter in front of the barrier islands.

The fine resolution model showed important new details compared to the coarse resolution model demonstrating that isolated islands (e. g. Helgoland), bathymetric channels and coastal topography off the estuary mouths supported development of small-scale patterns in the tidal spectrum. Unlike the case of the M_2 tide where maxima in M_2 amplitudes “followed” the bathymetric channels, M_4 amplitudes showed minima in the same areas. The latter patterns were also more “patchy” compared to the M_2 and had about one half the spatial scales. This gave a clear indication that it was not only the frequency that doubled in the M_4 tide but also the wave number.

The M_2 ellipses were aligned along the tidal channels, which was not the case with the M_4 ellipses. In many areas around the bathymetric channels the major axis of the M_4 ellipses was normal or at some angle with the major axis of the M_2 ellipses. This result illustrated that the higher harmonics tended to develop “orthogonal” patterns, which were important drivers for secondary circulation. Differently from the case of the M_4 tide, the non-linear friction mechanism described by the horizontal pattern of M_6 major axis surface currents was mostly located in the deep channels where velocities were strongest.

The pronounced spatial variability of spectra motivated the analysis of the differences between tidal responses during spring and neap situations. Of utmost importance was the result that the ratio between spring and neap amplitudes of sea level revealed different patterns. The spatial scales of this ratio were two times smaller for M_4 tides compared to the

M₂ tides. Furthermore, relatively low ratios were simulated for both tides in the Wadden Sea, showing less sensitivity of this very shallow area to neap-spring changes.

In the coastal ocean the bottom sediment characteristics are dependent on the tidal energy and tidal asymmetries, the latter are governed by the composition of tidal constituents. The agreement demonstrated here between the hydrodynamics and the observed sediment characteristics (Jansen et al. (2005) should help explain the physical mechanism shaping the pattern of median grain size in the German Bight.

Acknowledgements.

We are grateful to both referees for their comments on the first draft. Forcing data have been provided by German Weather Service. The bathymetric and river runoff data were provided by the Bundesamt für Seeschifffahrt und Hydrographie (BSH). Thanks to Alex Port for preparing the gridded model topography. BSH provided also the river run-off data. We acknowledge the use of Rapid Response imagery from the Land Atmosphere Near-real time Capability for EOS (LANCE) system operated by the NASA/GSFC/Earth Science Data and Information System (ESDIS) with funding provided by NASA/HQ. AVL acknowledges support from US NSF project OCE-0825876.

References:

- Allen, G. P., J. C. Salomon, P. Bassoullet, Y. Du Perthoat, and C. De Grandpre (1980), Effects of tides on mixing and suspended sediment transport in macrotidale estuaries. *Sediment. Geol.*, 26, 69-90.
- Andersen, O. B. (1999), Shallow water tides in the northwest European shelf region from TOPEX/POSEIDON altimetry, *J. Geophys. Res.*, 104(C4), 7729–7741, doi:[10.1029/1998JC900112](https://doi.org/10.1029/1998JC900112).
- Burchard, H. and Bolding K., 2002: GETM- a General Estuarine Transport Model. Scientific Documentation, 155.
- Carbajal, N., and J. H. Gaviño (2007), A new theory on tidal currents rotation, *Geophys. Res. Lett.*, 34, L01609, doi:[10.1029/2006GL027670](https://doi.org/10.1029/2006GL027670).
- Carbajal, N. and Pohlmann, T. (2004), Comparison between measured andcalculated tidal ellipses in the German bight. *Ocean Dynamics*, 54:520–530.
- Egbert, G. and S. Erofeeva (2002), Efficient inverse modeling of barotropic ocean tides. *Journal of Atmospheric and Oceanic Technology*, 19 (2), 183–204.
- Eichweber, G.; Lange, D. (1998), Tidal subharmonics and sediment dynamics in the Elbe Estuary, Proc. 3rd International Conf. On Hydrosience and Engineering, Cottbus/Berlin, 31.8–3.9.
- Fanjul, E., Gomez, B., Sanchez-Arevalo, I., 1997. A description of tides in the Eastern North Atlantic. *Progress in Oceanography* 40, 217–244.
- Friedrichs, C.T. (2010), Barotropic tides in channelized estuaries, *in*: Valle-Levinson, A. (Ed.) (2010). *Contemporary issues in estuarine physics*. Cambridge University Press, pp. 27-61.

Friedrichs, T. C. and Aubrey, D. G. (1988), Non-linear tidal distortion in shallow well mixed estuaries: a synthesis. *Estuarine, Coastal and Shelf Science*, 27:521–545.

Gallagher, B. S. and W. H. Munk (1971), Tides in shallow water: Spectroscopy. *Tellus*, 23, 346-363.

Ianniello, J. P. (1977), Tidally induced residual currents in estuaries of constant breadth and depth. *J. Mar. Res.*, 35, 755–786.

Janssen, F., Huettel, M., Witte, U. (2005), Pore-water advection and solute fluxes in permeable marine sediments (II): Benthic respiration at three sandy sites with different permeabilities (German Bight, North Sea). *Limnology and Oceanography*, 50, 779-792.

Jay, D. A. and Smith, J. D. (1990), Circulation, density distribution and neap-spring transitions in the columbia river estuary. *Progress in Oceanography*, 25:81–112.

Kappenberg, J. & H.-U. Fanger (2007), Sedimenttransportgeschehen in der tidebeeinflussten Elbe, der Deutschen Bucht und in der Nordsee. Gutachten GKSS 2007/20 des GKSS Forschungszentrums, Geesthacht GmbH, im Auftrag von Hamburg Port Authority. 125 pp.

Kappenberg, J., Schymura, G., and Fanger, H.-U. (1995), Sediment dynamics and estuarine circulation in the turbidity maximum of the Elbe river circulation in the turbidity maximum of the Elbe River. *Journal of Aquatic Ecology*, 24 (5):699-706.

Munk WH and Cartwright DE (1966), Tidal spectroscopy and prediction. *Philosophical Transactions of the Royal Society Series A* 259: 533–581.

Nichols, M. M., and R. B. Biggs (1985), Estuaries, in *Coastal Sedimentary Environments*, 2, nd ed., edited by R. A. Davis, pp. 77-186, Springer-Verlag, New York.

Parker, B. B. (1991), The relative importance of the various nonlinear mechanisms in a wide range of tidal interactions: In: Tidal hydrodynamics, ed. Parker, B.B. John Wiley & Sons, New York, 237-268.

Pawlowicz, R., B. Beardsley, and S. Lentz (2002), Classical tidal harmonic analysis including error estimates in MATLAB using T_TIDE", Computers and Geosciences 28, 929-937.

Plüß A, Schüttrumpf H (2004), Comparison of numerical tidal models for practical applications. Proceedings of the 29th Int. Conference of Coastal Engineering, pp 1199-1211

Port, A., Gurgel, K.W., Staneva, J., Schulz-Stellenfleth, J., Stanev, E.V. (2011), Tidal and wind-driven surface currents in the German Bight: HFR observations versus model simulations. Ocean Dynamics, 61:1567-1585.

Postma, H. (1984), Introduction to the symposium on organic matter in the Wadden Sea. Neth. Inst. Sea Res. Publ. Ser. 10, 15e22.

Le Provost, C. (1991), Generation of overtides and compound tides (Review). In: B.B. Parker (ed.). Tidal hydrodynamics. John Wiley & Sons, New York, pp. 269-295.

Pugh, D.T. (1996) *Tides, surges and mean sea-level (reprinted with corrections)*, Chichester, UK, John Wiley & Sons Ltd, 486pp.

Savcenko R., Bosch W. (2007), Residual tide analysis in shallow water - contributions of ENVISAT and ERS altimetry. In: Huguette Lacoste (ed): ENVISAT Symposium, ESA SP636.

Speer, P. E. 1984 Tidal distortion in shallow estuaries. PhD. thesis, WHOI-MIT Joint Program in oceanography, Woods Hole, MA, 210 pp.

Stanev, E. V., Flemming, B. W., Bartholomäa, A., and J. V. Staneva, J. O. W. (2007), Vertical circulation in shallow tidal inlets and back-barrier basins. *Continental Shelf Research*, 27:798-831.

Stanev, E. V., Schulz-Stellenfleth, J., Staneva, J., Grayek, S., Seemann, J., and Petersen, W. (2011), Coastal observing and forecasting system for the German Bight – estimates of hydrophysical states, *Ocean Sci.*, 7, 569-583.

Staneva, J., E. Stanev, J. Wolff, T. Badewien, R. Reuter, B. Flemming, A. Bartholomäa, and K. Bolding (2009), Hydrodynamics and sediment dynamics in the German Bight. A focus on observations and numerical modelling in the East Frisian Wadden Sea, *Cont. Shelf Res.*, 29(1), 302–319, doi:10.1016/j.csr.2008.01.006.

Zeiler M., J. Schulz.-Ohlberg , K. Figge (2000), Mobile sand deposits and shoreface sediment dynamics in the inner German Bight (North Sea). *Marine Geology*, 170, 3, 363-380.

Table 1: Location of the tide gauge station and current meter data used for model validation.

<i>Station Number</i>	<i>Station Name</i>	<i>Latitude</i>	<i>Longitude</i>
1	Bake Z	54.014 ⁰ N	8.315 ⁰ E
2	Bake A	53.984 ⁰ N	8.315 ⁰ E
3	Bake C Scharhorn	53.967 ⁰ N	8.462 ⁰ E
4	Mittelgrund	53.942 ⁰ N	8.636 ⁰ E
5	Cuxhaven	53.867 ⁰ N	8.717 ⁰ E
6	Jade	53.516 ⁰ N	8.13 ⁰ E
7	LZ ₄	53.938 ⁰ N	8.683 ⁰ E
8	Leuchtturm-Alte-Weser	53.8670 ⁰ N	8.1320 ⁰ E
9	Hooksielplate	53.6667 ⁰ N	8.13333 ⁰ E

Annex 1.

Table A1: Tidal constituents used to force the coarse resolution North Sea–Baltic Sea model

1	M2	Principal lunar semidiurnal constituent
2	S2	Principal solar semidiurnal constituent
3	N2	Larger lunar elliptic semidiurnal constituent
4	K1	Lunar diurnal constituent
5	O1	Lunar diurnal constituent
6	NU2	Larger lunar evectional constituent
7	MU2	Variational constituent
8	2N2	Lunar elliptical semidiurnal second-order constituent
9	Q1	Larger lunar elliptic diurnal constituent
10	T2	Larger solar elliptic constituent
11	P1	Solar diurnal constituent
12	L2	Smaller lunar elliptic semidiurnal constituent
13	K2	Lunisolar semidiurnal constituent

Annex 2. Tidal characteristics of the semidiurnal and diurnal tides.

Table A2: Tidal characteristics of the semidiurnal and diurnal tides.

Constituent	Station	M ₂	S ₂	K ₁	O ₁
<i>Amp_obs</i> (m)	Bake Z	1.334±0.043	0.492±0.044	0.0443±0.045	0.080±0.042
<i>Amp_mod_200</i> (m)		1.441±0.040	0.449±0.038	0.098±0.041	0.107±0.039
<i>Amp_mod_400</i> (m)		1.012±0.012	0.283±0.011	0.0410±0.012	0.056±0.012
<i>Pha_obs</i> (°)		280.20±2.13	21.28±4.99	348.00±54.66	201.76±33.43
<i>Pha_mod_200</i> (°)		286.84±1.58	7.92±5.95	319.83±23.98	208.05±21.17
<i>Pha_mod_400</i> (°)		333.01±0.63	42.08±2.67	361.32±16.18	255.53±12.15
Constituent	Station	M ₂	S ₂	K ₁	O ₁
<i>Amp_obs</i> (m)	Bake A	1.352±0.052	0.491±0.048	0.0410±0.040	0.100±0.046
<i>Amp_mod_200</i> (m)		1.456±0.041	0.452±0.036	0.098±0.038	0.107±0.041
<i>Amp_mod_400</i> (m)		1.028±0.012	0.284±0.012	0.041±0.013	0.056±0.011
<i>Pha_obs</i> (°)		279.00±2.08	20.90±6.09	359.28±69.29	207.49±28.47
<i>Pha_mod_200</i> (°)		286.29±1.67	7.51±5.39	323.36±24.88	207.35±19.89
<i>Pha_mod_400</i> (°)		332.59±0.60	41.52±2.69	360.00±17.23	255.121±12.74
Constituent	Station	M ₂	S ₂	K ₁	O ₁
<i>Amp_obs</i> (m)	Bake C	1.372±0.053	0.585±0.045	0.048±0.042	0.079±0.055
<i>Amp_mod_200</i> (m)		1.418±0.043	0.433±0.038	0.094±0.039	0.101±0.046
<i>Amp_mod_400</i> (m)		1.041±0.013	0.287±0.013	0.040±0.014	0.052±0.013
<i>Pha_obs</i> (°)		284.54±1.88	29.93±5.85	359.05±24.14	224.71±33.66
<i>Pha_mod_200</i> (°)		296.67±1.74	14.67±6.00	329.78±26.14	213.72±26.42
<i>Pha_mod_400</i> (°)		339.62±0.70	49.80±2.52	365.00±18.46	259.51±14.30
Constituent	Station	M ₂	S ₂	K ₁	O ₁
<i>Amp_obs</i> (m)	Mittelgrund	1.369±0.053	0.520±0.05	0.043±0.049	0.106±0.047
<i>Amp_mod_200</i> (m)		1.373±0.046	0.412±0.047	0.088±0.05	0.091±0.043
<i>Amp_mod_400</i> (m)		0.967±0.012	0.261±0.012	0.038±0.014	0.047±0.013
<i>Pha_obs</i> (°)		296.54±2.15	45.44±5.13	373.00±66.62	208.68±26.27
<i>Pha_mod_200</i> (°)		311.54±32.1	31.37±6.07	341.96±32.19	224.77±31.05
<i>Pha_mod_400</i> (°)		350.73±0.72	62.57±3.02	374±23.11	267.86±15.76
Constituent	Station	M ₂	S ₂	K ₁	O ₁
<i>Amp_obs</i> (m)	Cuxhaven	1.400±0.03	0.410±0.04	0.051±0.03	0.087±0.037
<i>Amp_mod_200</i> (m)		1.21±0.047	0.355±0.04	0.080±0.051	0.080±0.043
<i>Amp_mod_400</i> (m)		0.700±0.04	0.198±0.018	0.035±0.019	0.044±0.019
<i>Pha_obs</i> (°)		312.75±1.11	46.64±7.84	366±35.24	228.77±19.04
<i>Pha_mod_200</i> (°)		325.16±1.89	44.53±4.77	353.92±19.93	235.73±30.33
<i>Pha_mod_400</i> (°)		375.5±1.68	105.66±5.33	390±33.17	296.90±28.95
Constituent	Station	M ₂	S ₂	K ₁	O ₁
<i>Amp_obs</i> (m)	Hooksielplate	1.530±0.025	0.474±0.027	0.052±0.027	0.089±0.024
<i>Amp_mod_200</i> (m)		1.518±0.029	0.355±0.032	0.111±0.034	0.123±0.03
<i>Amp_mod_400</i> (m)		1.33±0.027	0.309±0.027	0.106±0.031	0.120±0.024
<i>Pha_obs</i> (°)		251.39±0.97	31.43±3.03	350.85±2.14	200.24±16.35
<i>Pha_mod_200</i> (°)		332.80±1.01	46.63±4.27	351.48±17.46	243.19±13.31
<i>Pha_mod_400</i> (°)		9	348.92±1.18	60.55±4.75	360.00±12.72

Constituent	Station	M₂	S₂	K₁	O₁
<i>Amp_obs (m)</i>	Leuchtturm-Alte-Weser	1.360±0.025	0.365±0.028	0.045±0.020	0.094±0.02
<i>Amp_mod_200(m)</i>		1.355±0.023	0.341±0.023	0.112±0.023	0.113±0.026
<i>Amp_mod_400(m)</i>		1.300±0.025	0.344±0.026	0.112±0.025	0.132±0.026
<i>Pha_obs (°)</i>		239.38±1.00	18.54±3.49	359.00±33.67	158.78±14.68
<i>Pha_mod_200(°)</i>		292.99±1.14	358.27±4.75	327.46±11.73	220.80±8.90
<i>Pha_mod_400(°)</i>		317.95±1.02	23.75±4.08	340.21±13.05	232.60±11.60

Table A3: Tidal characteristics of the *over tides and compound tides*.

Constituent	Station	M ₄	M ₆	MSF	MS ₄
<i>Amp_obs</i> (m)	Bake Z	0.075±0.040	0.022±0.036	0.094±0.046	0.074±0.045
<i>Amp_mod_200</i> (m)		0.075±0.043	0.026±0.043	0.09±0.044	0.059±0.039
<i>Amp_mod_400</i> (m)		0.019±0.011	0.004±0.009	0.011±0.011	0.011±0.011
<i>Pha_obs</i> (°)		79.64±35.04	247.24±107.2	126.41±29.0	161.56±37.09
<i>Pha_mod_200</i> (°)		73.18±34.29	235.61±88.26	169.00±18.8	140.65±39.05
<i>Pha_mod_400</i> (°)		86.70±33.50	270.30±46.70	177.24±59.8	168.54±62.84
Constituent	Station	M ₄	M ₆	MSF	MS ₄
<i>Amp_obs</i> (m)	Bake A	0.077±0.05	0.027±0.039	0.083±0.045	0.061±0.049
<i>Amp_mod_200</i> (m)		0.072±0.038	0.026±0.033	0.094±0.042	0.053±0.039
<i>Amp_mod_400</i> (m)		0.025±0.012	0.01±0.01	0.0134±0.01	0.011±0.011
<i>Pha_obs</i> (°)		88.33±33.82	250.45±112.3	140.48±31.9	175.90±42.83
<i>Pha_mod_200</i> (°)		71.72±31.34	235.46±92.65	170.11±19.4	138.48±42.63
<i>Pha_mod_400</i> (°)		75.42±29.32	270.47±39.30	172.2±53.14	155.85±59.80
Constituent	Station	M ₄	M ₆	MSF	MS ₄
<i>Amp_obs</i> (m)	Bake C	0.067±0.05	0.01±0.033	0.136±0.051	0.055±0.042
<i>Amp_mod_200</i> (m)		0.076±0.041	0.034±0.042	0.142±0.039	0.058±0.037
<i>Amp_mod_400</i> (m)		0.032±0.012	0.01±0.01	0.022±0.012	0.017±0.013
<i>Pha_obs</i> (°)		97.07±42.39	313.69±148.3	130.83±17.3	233.76±59.67
<i>Pha_mod_200</i> (°)		84.23±33.89	319.00±50.19	169.65±18.0	152.05±41.30
<i>Pha_mod_400</i> (°)		98.05±21.24	205.50±36.26	177.36±36.8	182.62±41.67
Constituent	Station	M ₄	M ₆	MSF	MS ₄
<i>Amp_obs</i> (m)	Mittel-Grund	0.073±0.05	0.0204±0.036	0.078±0.046	0.042±0.052
<i>Amp_mod_200</i> (m)		0.106±0.047	0.052±0.039	0.097±0.047	0.074±0.043
<i>Amp_mod_400</i> (m)		0.047±0.013	0.012±0.012	0.031±0.013	0.027±0.011
<i>Pha_obs</i> (°)		116.42±39.93	301.75±128.3	175.72±34.4	223.69±65.97
<i>Pha_mod_200</i> (°)		109.90±23.90	291±46.82	166.12±15.7	180.37±30.04
<i>Pha_mod_400</i> (°)		138.64±15.51	212.08±27.38	175.33±22.	222.14±24.88
Constituent	Station	M ₄	M ₆	MSF	MS ₄
<i>Amp_obs</i> (m)	Cuxhave-n	0.102±0.03	0.045±0.052	0.150±0.047	0.087±0.051
<i>Amp_mod_200</i> (m)		0.091±0.046	0.058±0.039	0.151±0.042	0.064±0.037
<i>Amp_mod_400</i> (m)		0.016±0.018	0.025±0.023	0.015±0.012	0.012±0.012
<i>Pha_obs</i> (°)		155.55±25.49	324.84±70.83	110±20.49	241.15±31.02
<i>Pha_mod_200</i> (°)		136.98±27.26	322.76±46.68	163.78±17.7	202.66±42.01
<i>Pha_mod_400</i> (°)		179.41±67.78	290.00±17.36	109.89±17.2	316.45±85.22
Constituent	Station	M ₄	M ₆	MSF	MS ₄
<i>Amp_obs</i> (m)	Hooksiel-plate	0.100±0.02	0.058±0.026	0.030±0.020	0.078±0.024
<i>Amp_mod_200</i> (m)		0.118±0.028	0.089±0.03	0.072±0.03	0.06±0.03
<i>Amp_mod_400</i> (m)		0.122±0.026	0.057±0.026	0.074±0.029	0.063±0.026
<i>Pha_obs</i> (°)		193.88±21.76	64.50±21.50	197.94±52.2 8	110.50±17.60
<i>Pha_mod_200</i> (°)		126.00±12.05	58.0 ±18.64	144.10±21.0 0	185.43±27.02
<i>Pha_mod_400</i> (°)		193.14±12.81	4.96±23.79	145.86±20.7 8	200.43±24.35
Constituent	Station	M ₄	M ₆	MSF	MS ₄
<i>Amp_obs</i> (m)		0.070±0.024	0.048±0.024	0.036±0.022	0.048±0.024

<i>Amp_mod_200(m)</i>	Leuchtturm- Alte- Weser	0.0629±0.026	0.032±0.023	0.062±0.028	0.0413±0.026
<i>Amp_mod_400(m)</i>		0.074±0.028	0.0347±0.023	0.072±0.023	0.048±0.025
<i>Pha_obs (°)</i>		159.00±14.68	74.27±27.643	33.01±37.84	122.19±25.73
<i>Pha_mod_200(°)</i>		80.00±20.54	242±49.12	149.75±18.8 0	146.55±34.45
<i>Pha_mod_400(°)</i>		148.00±0.028	325±40.70	152.70±16.8 4	190±35.60

Annex 4.

Table A4: Major axes current analysis

		<u>Observed</u>		<u>Model 200m</u>		<u>Model 400m</u>	
	Station	<i>Major (m/s)</i>	<i>Phase (degree)</i>	<i>Major (m/s)</i>	<i>Phase (degree)</i>	<i>Major (m/s)</i>	<i>Phase (degree)</i>
M₂	LZ₄	0.526	330	0.517	311	0.156	317
M₄		0.078	232	0.048	200	0.018	94
M₆		0.039	132	0.048	190	0.022	127

		<u>Observed</u>		<u>Model 200m</u>		<u>Model 400m</u>	
	Station	<i>Major (m/s)</i>	<i>Phase (degree)</i>	<i>Major (m/s)</i>	<i>Phase (degree)</i>	<i>Major (m/s)</i>	<i>Phase (degree)</i>
M₂	Jade	0.420	222.99	0.581	238.45	0.389	228.29
M₄		0.170	12.33	0.140	6.37	0.072	41.44
M₆		0.100	252.89	0.113	200	0.012	239

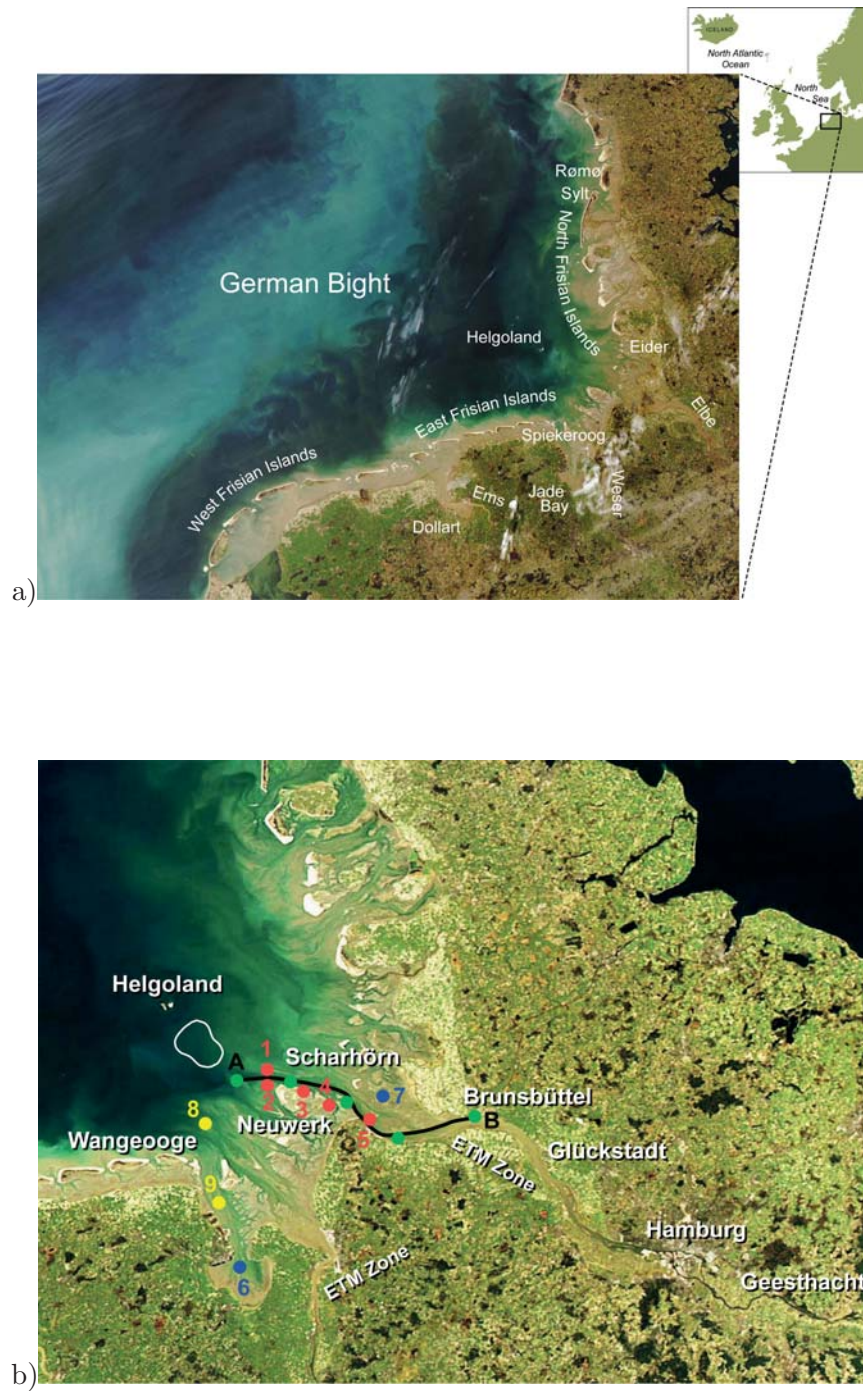


Figure 1: (a) North Sea and German Bight. The image is of Aqua/MODIS 03/09/2014, 11:50 UTC showing the sediment in the North Sea (the North-Frisian front is well seen). Some geographical names used in the text are added. (b) is the same but for 03/12/2014, 12:20 UTC in the estuarine region. Locations where analysis of observations and numerical simulations are presented in the text are identified on the map.

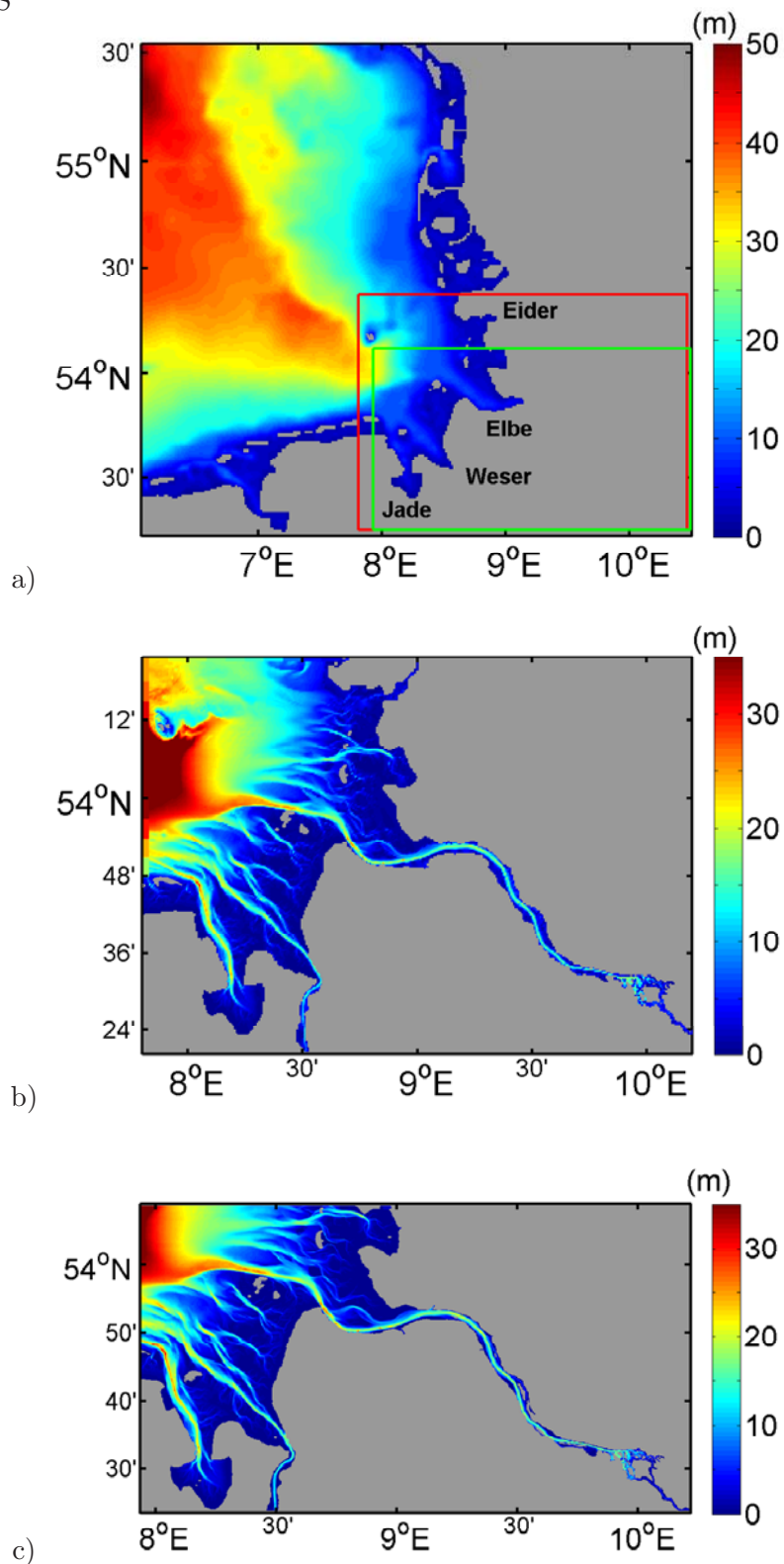


Figure 2: (a) Bathymetry of the German Bight (in m) as used in the 1 km resolution model. (b) and (c) is the same but only for the south-eastern part resolved with a horizontal grid of 400 and 200 m, respectively (red and green boxes in (a)). Insets in (b) and (c) demonstrate how the fine scale topographies are seen with the different resolution used.

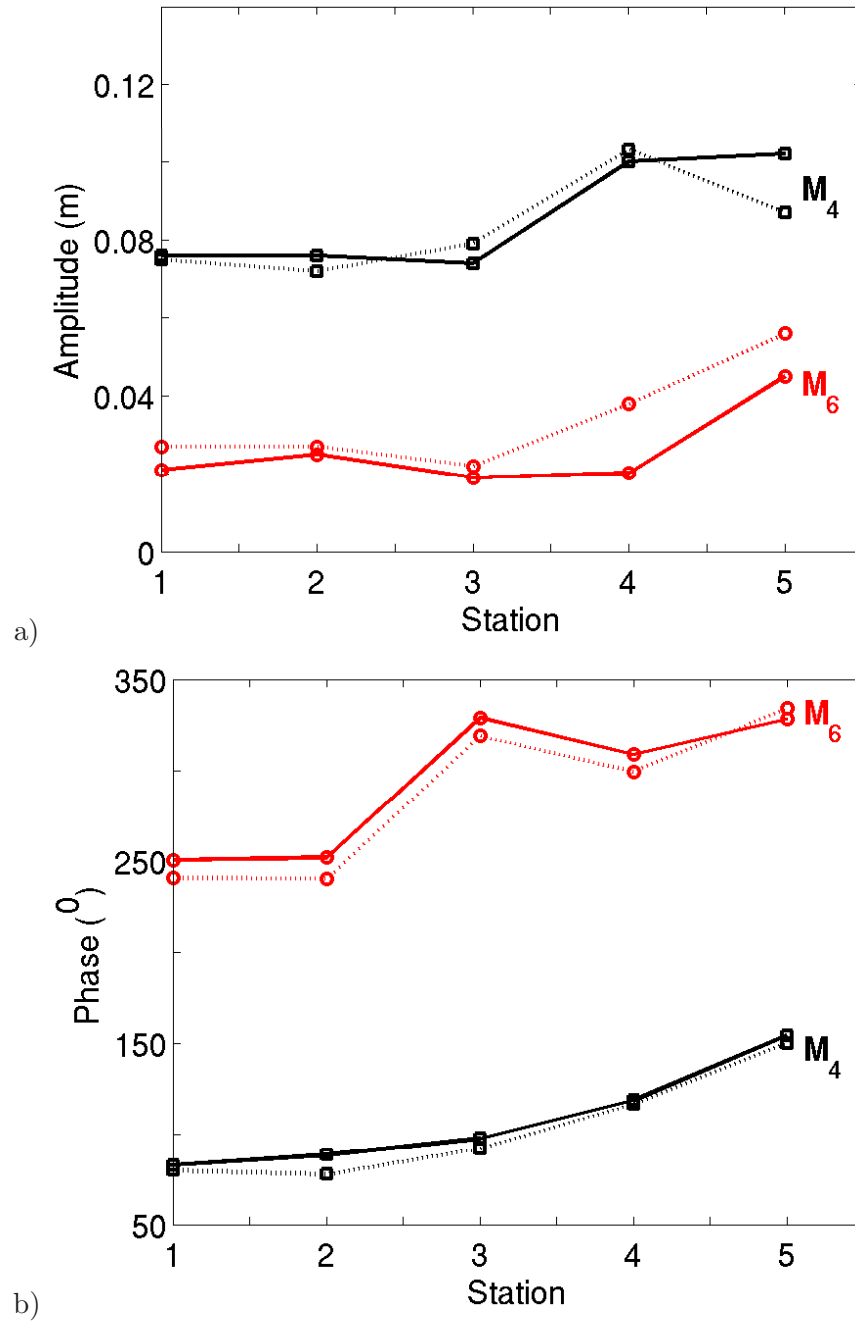


Figure 3: Amplitudes (upper panel) and phases (bottom panel) of the major overtones. The simulations from the 200 m resolution model and observations are shown with dotted and full lines, respectively. The analysis is for 03/04/2011 to 20/04/2011. The positions of stations are given in Fig. 1b.

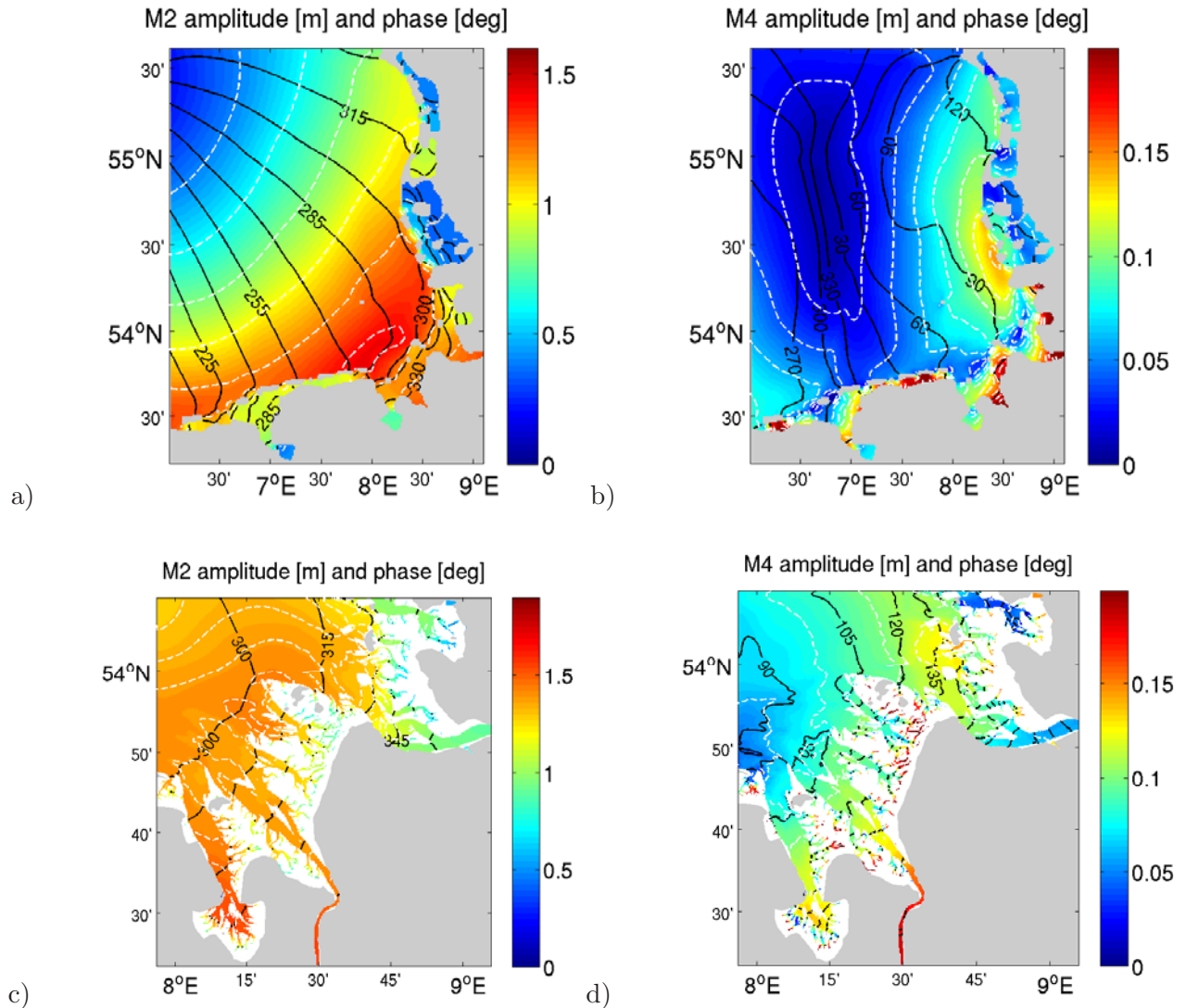


Figure 4: Phase lines (black) and co-ranges (in m, see the colour bar) simulated in the model with 1 km resolution (a, b) and 200 resolution (c, d) for April/May 2011. (a) and (c) display the M2 patterns; (b) and (d) the M4 ones. The over-imposed white dashed lines reveal more clearly the horizontal patterns of ranges: from 0.4 m to 1.5 m with steps of 0.2 m in (a); from 1.1 m to 2 m with steps of 0.04 m in (c); from 0 m to 0.2 m with steps of 0.02 m in (b and d). Tidal analysis has been performed only in areas not undergoing drying in order to avoid working with non-homogeneous data sets. This is the reason why in this and some of the following figures tidal flats are blanked white.

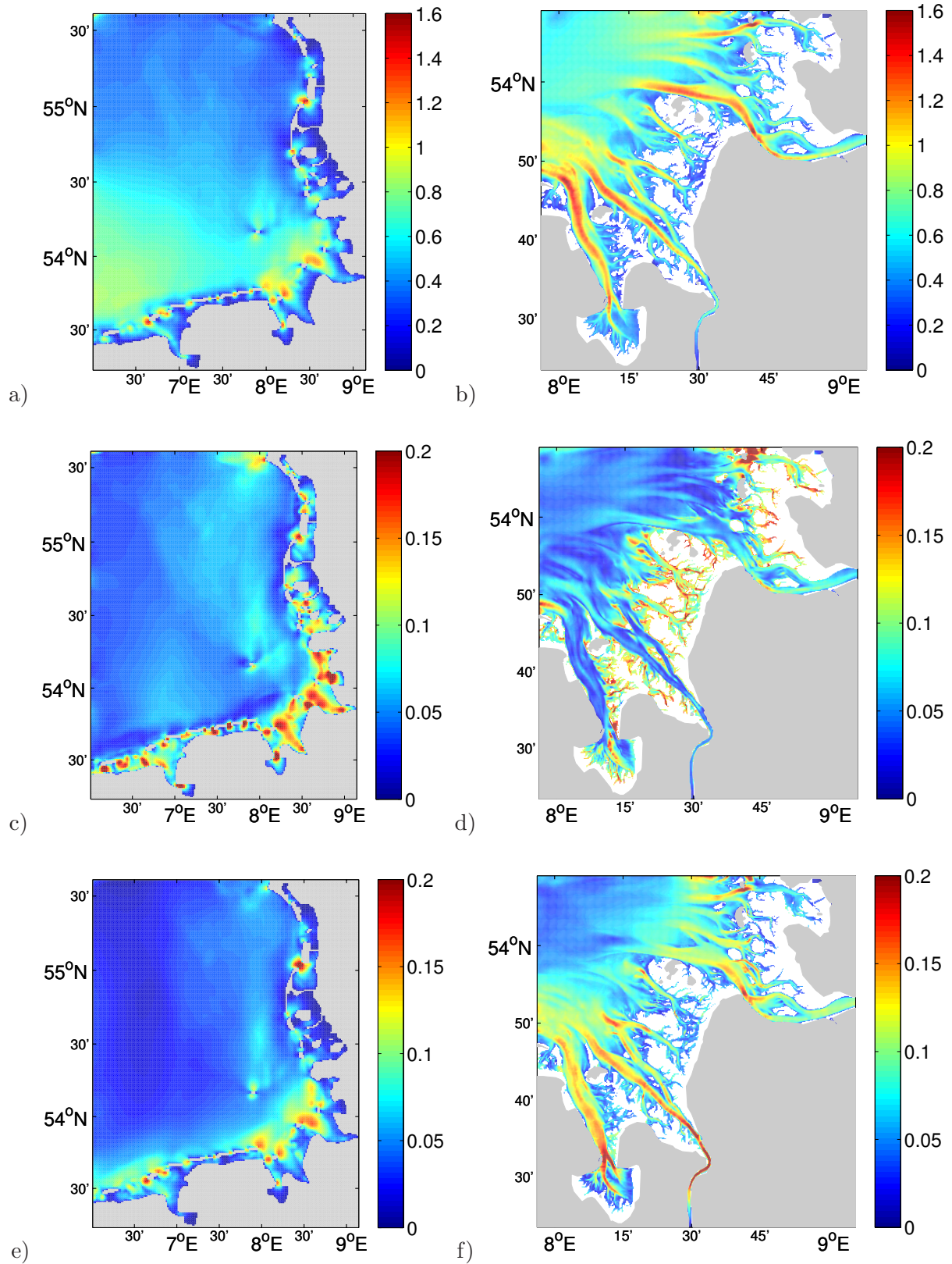


Figure 5: Amplitudes in (m/s) of the major axes currents in 1 km (a, c, d) and 200 m (b, d, f) resolution models for spring tide periods in April/May 2011. Three tidal constituents are presented: M2 (a, b), M4: (c, d), M6 (e, f). In the white areas (shallower than 0.8 m), which fall dry during relatively long time, tidal analysis has not been performed to avoid possible misinterpretations due to the inhomogeneity of data series.

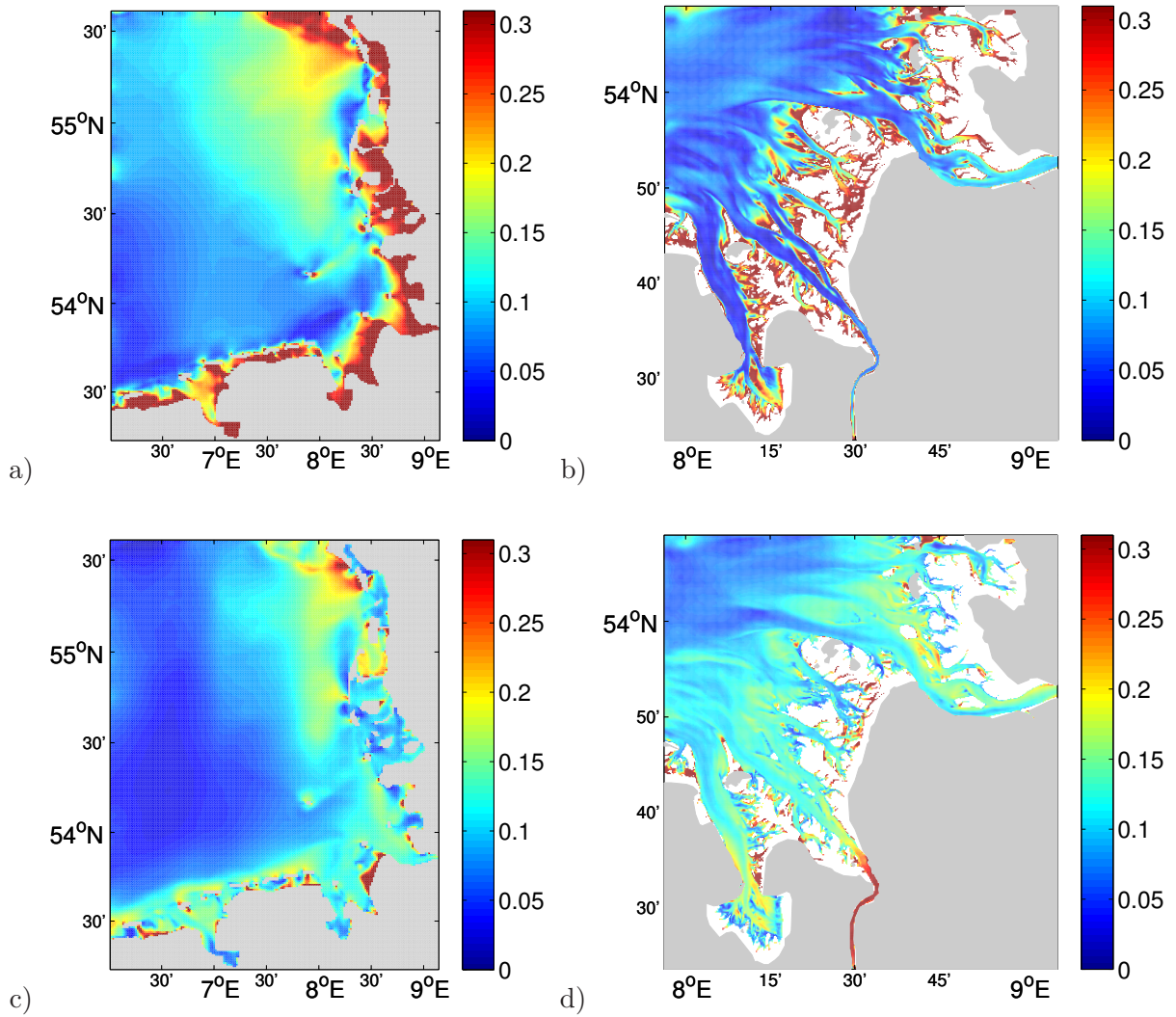


Figure 6: The ratio between amplitudes of M4 and M2 (a, b) and M6 and M2 tidal currents (c, d) for spring tide periods in April/May 2011. (a) and (c) from the simulations with the model with 1 km horizontal resolution; (b) and (d) correspond to 200 m resolution model.

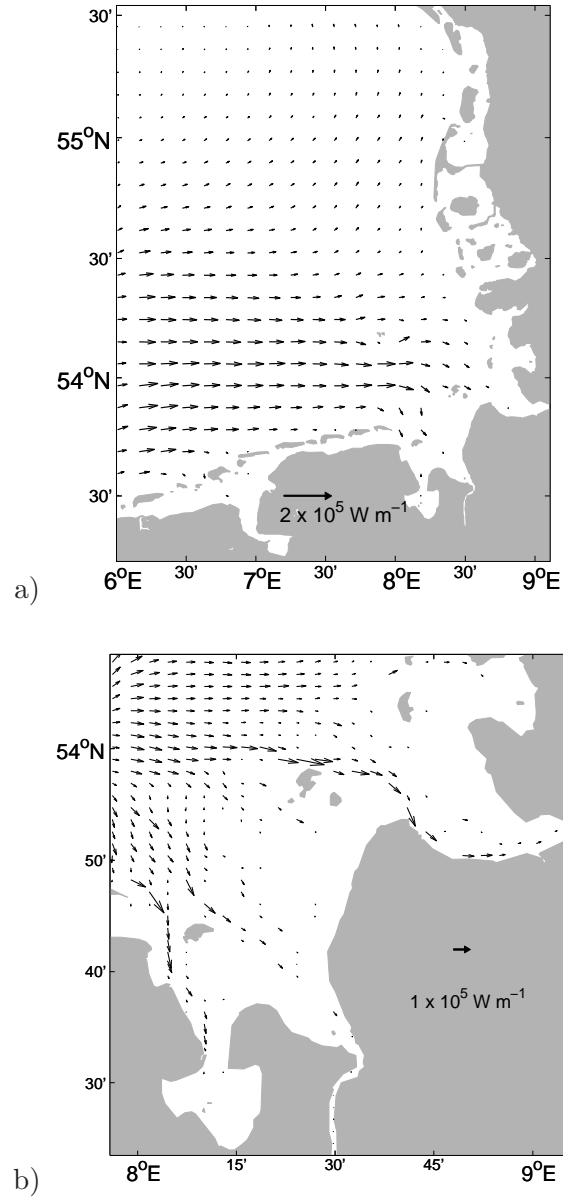


Figure 7: Transport of energy of M2 tide from the simulations with the model with 1 km horizontal resolution (a) and 200 m resolution model (b).

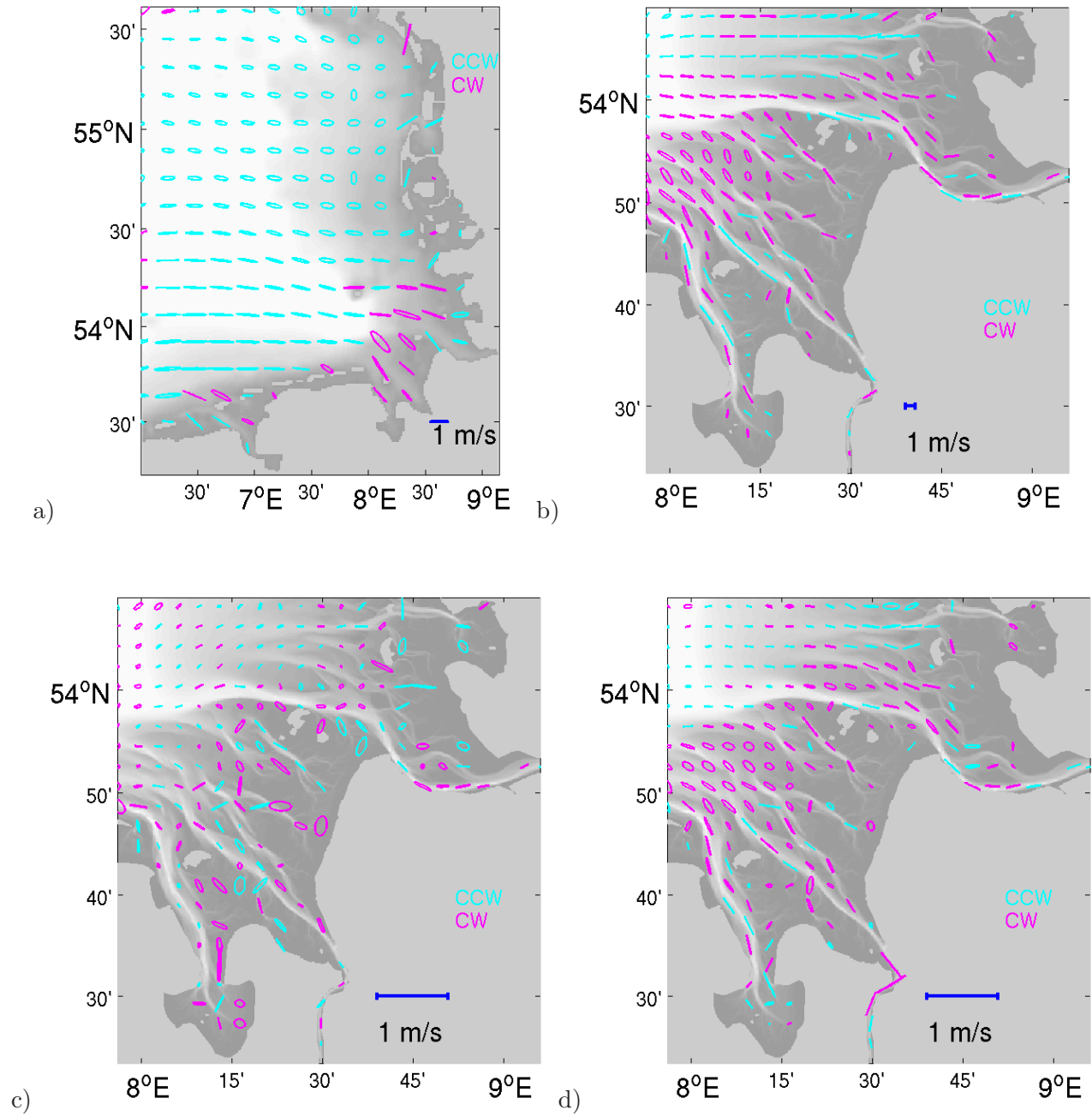


Figure 8: Tidal ellipses for spring tide periods in April/May 2011. (a) M2 tide in the 1 km resolution model, (b, c, d) M2, M4 and M6 tide in 200 m resolution model . Grey shading shows topography, the blue ellipses correspond to counter clockwise (CCW) rotation, the magenta ones to clockwise (CW) rotation.

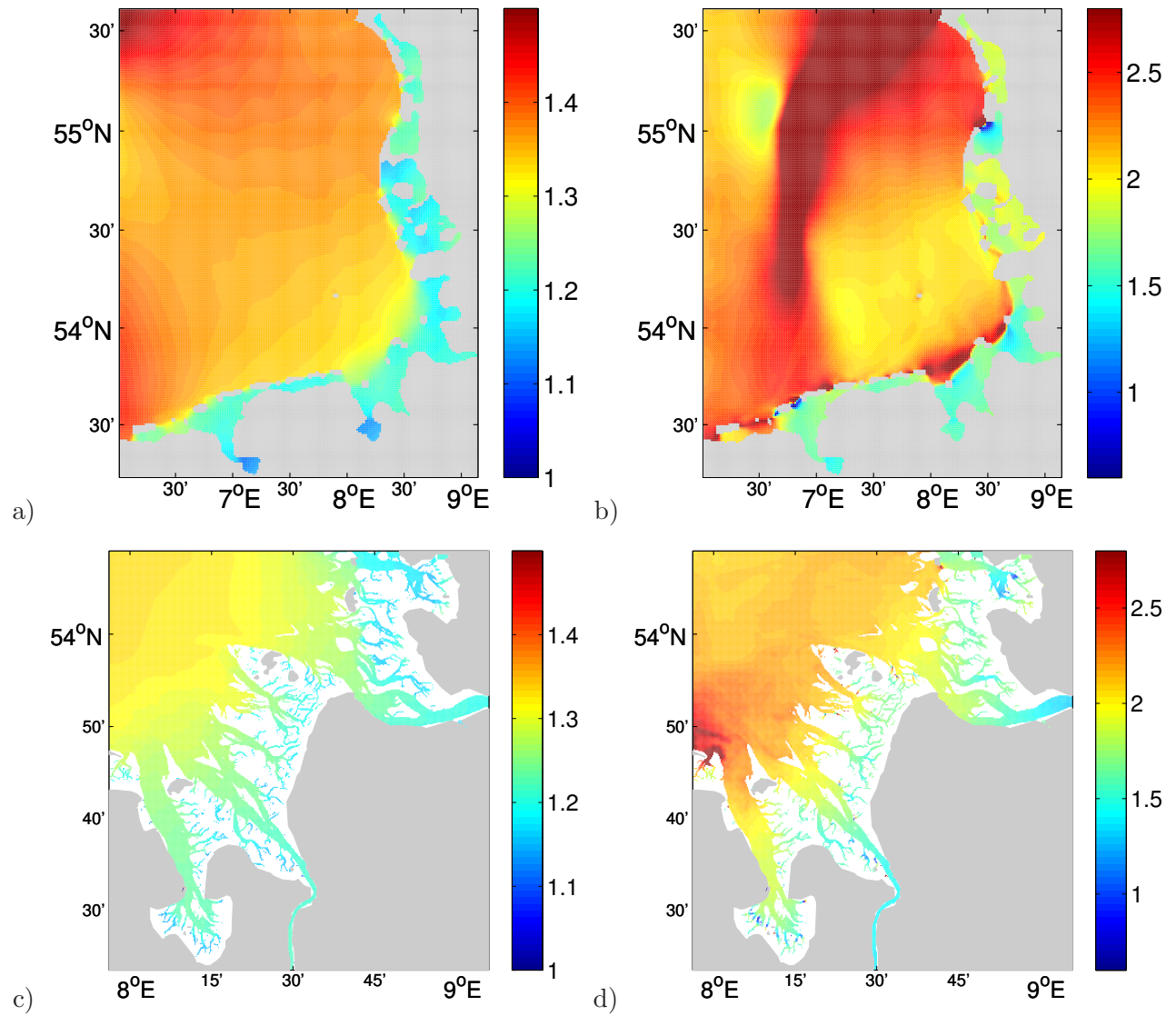


Figure 9: The ratio between spring and neap M2 (a, c) and M4 (b, d) sea level amplitudes for 1 km resolution domain (a, b) and 200 m resolution domain (c, d).